Raman and X-Ray Scattering Studies of High-Pressure Phases of Urea

F. J. Lamelas, Z. A. Dreger,* and Y. M. Gupta

Institute for Shock Physics and Department of Physics, Washington State University, Pullman, Washington 99164-2816

Received: December 15, 2004

Single-crystal and polycrystalline urea samples were compressed to 12 GPa in a diamond-anvil cell. Raman-scattering measurements indicate a sequence of four structural phases occurring over this pressure range at room temperature. The transitions to the high-pressure phases take place at pressures near 0.5 GPa (phase I → II), 5.0 GPa (II → III), and 8.0 GPa (III → IV). Lattice parameters in phase I (tetragonal, with 2 molecules per unit cell, space group $P\bar{4}2_1m$ (D_{2d}^3)) and phase II (orthorhombic, 4 molecules per unit cell, space group $P2_12_12_1$ (D_2^4)) were determined using angle-dispersive X-ray diffraction experiments. For phases III and IV, the combined Raman and diffraction data indicate that the unit cells are likely orthorhombic with four molecules per unit cell. Spatially resolved Raman measurements on single-crystal samples in phases III and IV reveal the coexistence of two domains with distinct spectral features. Physical origins of the spatial domains in phases III and IV are examined and discussed.

1. Introduction

Hydrogen bonding is one of the most important and extensively studied intermolecular interactions in molecular crystals. Urea is a prototypical hydrogen-bonded molecular crystal of significant scientific and practical importance.[1,2] Because of its simple structure, urea can be considered as a model system for studying the structure and phase stability of hydrogen-bonded molecular solids. In this study, we use high pressures to examine and understand the effects of intermolecular interactions on the stability of the urea crystal structure.

At ambient temperature and pressure, urea crystallizes in a noncentrosymmetric tetragonal structure, with lattice parameters $a = 5.661$ Å and $c = 4.712$ Å, and space group $P\bar{4}2_1m$ (D_{2d}^3). As shown in Figure 1, ribbons of planar $CO(NH_2)_2$ molecules are linked head-to-tail, parallel to the *c*-axis, with neighboring ribbons containing oppositely oriented molecules rotated 90° about the *c*-axis.[3] Each oxygen atom participates in four hydrogen bonds; the overall structure that results from the optimization of these bonds is quite open, as seen in the upper panel of Figure 1. The electric dipole moment of the molecule in solution has a fairly large value, 4.56 D.[4] It has been demonstrated that urea is an excellent nonlinear optical crystal for second-harmonic generation and sum frequency mixing in the ultraviolet (to 238 μm), with a higher efficiency than the well-known KDP isomorphs.[5,6]

There are relatively few published reports on the high-pressure properties of urea. In 1916, using volumetric techniques with polycrystalline samples in mercury, Bridgman reported a transition to a high-pressure phase at 0.5 GPa.[7] This same phase I → II transition was noted more recently in limited infrared[8] and Raman[9] studies. Through the use of piston cells capable of reaching approximately 1.5 GPa, it has been observed that the thermal conductivity of urea drops by 20% at the phase boundary[10] and the volume drops by 7%,[11] indicating that a significant rearrangement of the structure occurs during the I → II phase transition. In another study, the efficiency of second-harmonic generation (SHG) in urea was measured to 8.5 GPa,

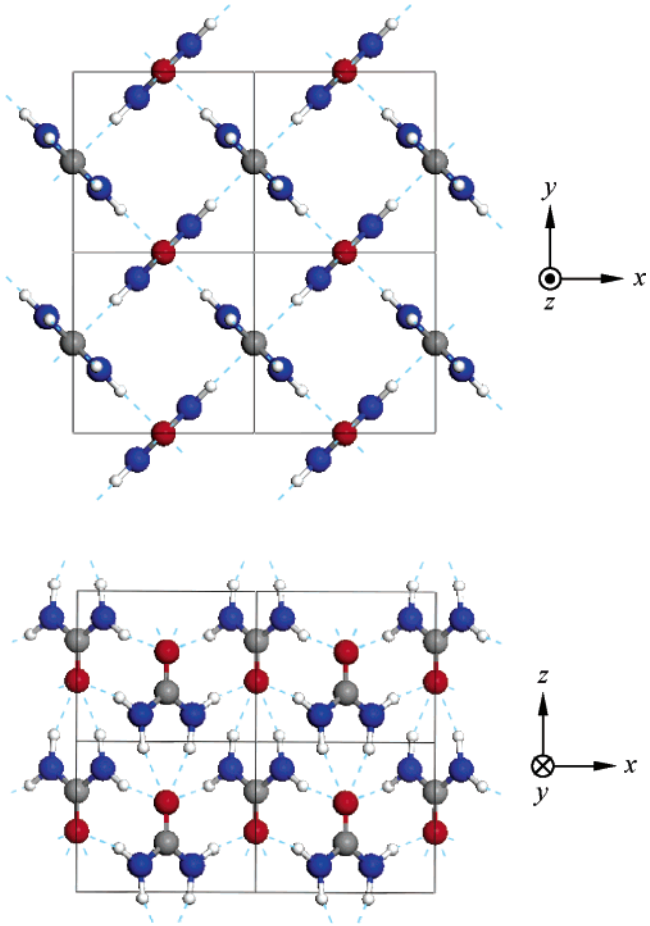

Figure 1. Ambient-pressure structure of urea, $CO(NH_2)_2$. Gray, red, blue, and white spheres correspond to C, O, N, and H, and hydrogen bonds are shown as dashed blue lines. In the lower panel, the planes of the molecules are inclined at 45° to the viewing direction.

* Author to whom correspondence should be addressed. E-mail: dreger@wsu.edu.

10.1021/jp040760m CCC: $30.25
Published on Web 04/02/2005

using a diamond-anvil cell (DAC).[12] For single crystals, a sharp peak in the efficiency was found at 0.5 GPa, coincident with the phase transition, and a broader maximum occurred near 4.5 GPa. Most recently, neutron-scattering studies of polycrystalline deuterated urea in a Paris−Edinburgh high-pressure cell have led to a solution of the phase II structure.[13] With improved sample gasketing, Marshall and Francis[14] have performed neutron measurements to 8.5 GPa, detecting two new structural phases that appear at 3.0 and 7.5 GPa, i.e., they observe four total phases of deuterated urea (urea-d_4), which we denote as phases I−IV.[15]

Urea was chosen as the subject of these experiments on the basis of its importance as a model hydrogen-bonded system. We report a series of Raman-scattering measurements on urea in a DAC at room temperature, at pressures up to 12 GPa. Both lattice (intermolecular) modes and internal (intramolecular) modes were examined in experiments on single-crystal and powder samples. The Raman experiments also included spatially resolved measurements that were used to generate maps of the Raman spectra for single crystals at high pressure. X-ray diffraction measurements were carried out on a polycrystalline sample to directly probe the structure of the high-pressure phases over a similar pressure range.

2. Experimental Details

Urea crystals were prepared by first dissolving urea powder (Aldrich, 99%+) in methanol (spectrophotometric grade, 99.9%). Slow evaporation led to the formation of crystals that were approximately 20 mm long in the *c*-axis direction.[16] For single-crystal measurements, as-grown crystals were cleaved to form platelets with dimensions of approximately 100 μm × 100 μm × 25 μm, with the plane of the samples parallel to the {110} cleavage planes. Powder samples were prepared by grinding single crystals in a mortar.

High pressures were generated in a Merrill−Bassett-type DAC,[17] using a 200 μm in diameter sample chamber in stainless steel gaskets preindented to a thickness of approximately 100 μm. Eleven total runs were carried out; in nine cases, cryogenically loaded Ar was the pressure medium, one run was carried out using N_2, and one with mineral oil. A small ruby chip was loaded with each sample to monitor the pressure using the ruby fluorescence scale.[18,19] The resolution of the pressure measurements is approximately 0.05 GPa.

Raman spectra were acquired using the 514.5 nm line from an Ar-ion laser as an excitation source. The laser beam was passed through a vertical polarizer and a tunable filter, then focused onto the sample using a microscope objective with a long focal length. The backscattered light was dispersed with a triple spectrometer equipped with a liquid-nitrogen-cooled charge-coupled, device (CCD). Neither a polarization analyzer nor a scrambler was used in the scattered beam. We carried out individual DAC runs using a fixed spectrometer setting with a 1200 cm^{-1} range; the entire Raman spectrum was studied as a function of pressure by performing multiple DAC pressure runs. The spectral resolution of the Raman system is approximately 1 cm^{-1}, and in all cases Raman peak positions were obtained by fitting the spectra to sums of Gaussian and Lorentzian peaks. Additional details regarding the pressure calibration and Raman system are presented in ref 20.

During the Raman measurements, the DAC was mounted on a three-axis translation stage with micrometer drives. The spatial resolution limit is determined by the spot size of the incident laser beam in the DAC. From the measurement of the in-situ Raman-scattering intensity while the edge of a sample in a DAC was translated relative to the beam, we estimate that the spot size is approximately 5 μm. The data used in the spatial maps presented in section 3.4 were collected by measuring spectra on a 20 μm grid. Therefore, the resolution of our spectral maps is determined by the spatial sampling interval and not the incident-beam spot size.

A polycrystalline sample was mounted in a piston-type DAC for synchrotron X-ray diffraction measurements, using Ar as a pressure medium and gaskets similar to those described above. Ruby fluorescence was again used for pressure calibration. Angle-dispersive diffraction measurements were carried out on the High Pressure Collaborative Access Team (HPCAT) beamline (16 ID-B) at the Advanced Photon Source, Argonne National Laboratory.[21] A monochromatic 0.368 Å beam with a diameter of 10 μm was incident on the sample. To improve the uniformity of the diffracted cones of radiation, the sample was continuously rastered over a range of 100 μm × 100 μm, transverse to the incident X-ray beam, to illuminate as many individual crystallites as possible. The scattered radiation was collected with an image-plate area detector. Any intense diffraction peaks due to the pressure-cell diamonds were masked, and the remaining two-dimensional pattern was integrated to obtain a one-dimensional powder-diffraction pattern. The peak positions were determined by fitting the pattern with a combination of Gaussian and Lorentzian functions. These were then entered into the powder-diffraction autoindexing programs, DICVOL91 and McMaille, to obtain crystallographic unit-cell parameters.[22] Candidate space groups were obtained using a commercial software package.[23]

3. Results and Discussion

Figure 2 shows typical Raman spectra obtained from urea single crystals at pressures ranging from ambient to 9.5 GPa. Six different Raman patterns were observed over four pressure ranges (I → IV). In the lower two ranges (phases I and II), the same spectrum is obtained over the entire sample. In the upper ranges (phases III and IV), two distinct spectra (labeled A and B) were often observed in different regions of a given sample. We refer to the coexisting spatial regions as domains III-A and III-B (in the third pressure range) and IV-A and IV-B (in the fourth range). The Raman and X-ray scattering data, obtained in each of the four pressure ranges, are presented in the following subsections.

3.1. Phase I. A representative ambient-pressure spectrum in the 0−1200 cm^{-1} range is shown as the lowest plot in Figure 2, and a summary of all Raman-active modes is presented in Table 1. At ambient pressure, our lattice-mode frequencies are in good agreement with earlier experimental data.[24] The measured frequencies are reproduced fairly well by a model[25] that utilizes a phenomenological Buckingham-type potential. However, a first-principles density functional theory (DFT) calculation does not match the measured frequencies as well.[26] The pressure dependence of the lattice modes, $d\nu/dP$, (Table 1, last column) was obtained by combining data from two separate runs, as shown in Figure 3. The B_1 mode, assigned to a *c*-axis libration,[24] shows almost no pressure dependence, in comparison to the E modes.

The internal modes of the ambient structure of urea serve as an interesting example where intermolecular coupling is clearly seen in vibrational spectra.[27] As shown in Table 1, our spectral frequencies agree quite well with previous data[28] and with calculations performed recently with a molecular cluster model.[29] In the following presentation of high-pressure data, we assume that qualitative physical assignments of vibrational modes can

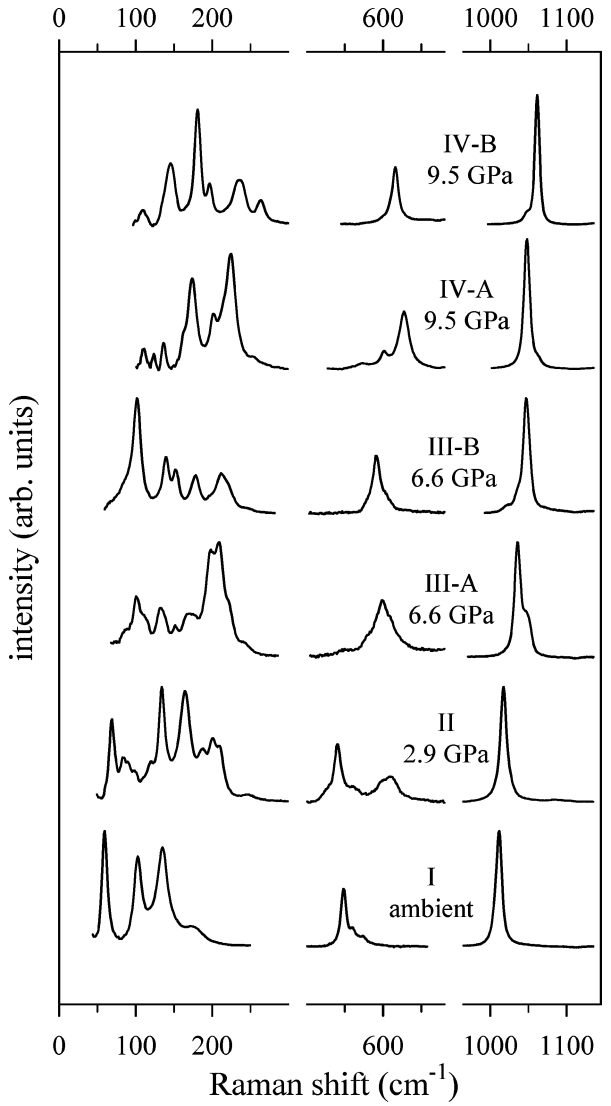

Figure 2. Typical Raman data for six different urea structures, with intensities normalized to allow comparison of all vibrational modes. The partial spectra shown here were collected with a single setting of the spectrometer.

be made based on the penultimate column of Table 1, i.e., lattice modes occur below 300 cm^{-1}, C−N bending modes occur near 600 cm^{-1}, C−N stretching modes near 1025 cm^{-1}, and N−H stretching modes near 3400 cm^{-1}.

3.2. Pressure Dependence and Evidence for Phase Transformations. Figure 4 is a plot of Raman frequencies from ambient pressure to approximately 12 GPa. Significant changes in the spectra occur at the pressures marked by dashed lines; the four pressure ranges bounded by the dashed lines are labeled I−IV. The I → II transition was observed by Bridgman,[7] and the subsequent ones near 4.6 and 8.2 GPa are presumably those observed in neutron-scattering experiments on deuterated urea (ref 14). The number of Raman-active modes at a given pressure is in general larger than the number plotted in Figure 4 because we have shown only a selected subset of modes. Only those modes that were unambiguously present across a broad range of pressures are shown in Figure 4. As seen in the figure, the II → III and III → IV phase transitions were somewhat gradual, often occurring over a range of 1−1.5 GPa. Occasionally, when the pressure was adjusted close to a phase boundary, the spectra were observed to evolve gradually from one phase to the next over the course of 1−2 h.

In the two higher-pressure ranges (III and IV), we often observed segregation of the sample into pairs of domains with distinct spectral features (III-A and III-B, and/or IV-A and IV-B). To identify phase transitions as a function of pressure, the clearest case to examine is a run that does *not* show domain segregation in phases III and IV. In this case, there is only a single spectrum to consider in each pressure range (either A or B) rather than a combination of two spectra. Such an example is shown in Figure 4, which corresponds to a sample that followed the sequence I → II → III-B → IV-A. The specific A/B assignment of the spectra may be checked by comparing the features in Figure 4 (both frequencies and intensities) to the typical spectra in Figure 2. In general, our assignment of a phase III or IV spectrum as either type A or B is based on the relative intensities in a doublet of C−N stretching modes near 1025 cm^{-1}. As indicated by the upper four plots in Figure 2, if the lower-frequency mode is stronger, then the spectrum is denoted as an A type, if otherwise, then a B type. This criterion is arbitrary but is convenient experimentally since the distribution of intensities across the doublet is immediately obvious when viewing a spectrum in real time during sample alignment.

We expected the N−H stretching modes to be sensitive to structural rearrangement in a hydrogen-bonded crystal. Indeed, clear signatures of the phase transitions are seen in Figure 5, which contains data from a different DAC run than that shown in Figure 4. In this case, the phase boundaries appear near 5.2 and 8.0 GPa. In phase I, an antisymmetric N−H stretching mode exhibits a negative slope for $d\nu/dP$ (Table 1, last column). This implies that hydrogen bonding (H···O) becomes stronger with increasing pressure. A significantly negative slope also occurs in phase III, as seen in Figure 5.

Figure 6 shows X-ray diffraction data for a polycrystalline sample in the four pressure ranges. We were able to index the reflections for phases I and II using autoindexing software.[22] At ambient pressure, phase I served as a test case and was indexed with a tetragonal unit cell with lattice parameters (Table 2) that match published values[3] to 0.25%. As shown below, phase II was indexed with an orthorhombic unit cell, in close agreement with recent neutron-scattering results.[13] Our X-ray patterns for phases III and IV could not be indexed unambiguously, presumably due to limitations in the data, since the autoindexing programs generally require precise peak positions for 15−20 reflections. As seen in Figure 6, with an increase in pressure the diffraction peaks broaden somewhat, making it more difficult to resolve weaker peaks. In addition, the argon pressure medium solidifies at 1.15 GPa,[31] and strong scattering near the argon Bragg reflections leads to breaks in the accessible portion of the urea pattern. Finally, if the A/B domains in phases III and IV correspond to different crystal structures, the autoindexing programs would fail, since they require input corresponding to a single phase. Although phase III and IV diffraction peaks have not been indexed, qualitative differences in the patterns indicate that they correspond to distinct structures. Therefore, the X-ray data as a whole serve to corroborate the existence of phases I−IV, determined from the Raman measurements.

3.3. Phase II. The well-known I → II phase transition occurs at approximately 0.5 GPa.[7−14] However, published structural data on phase II are quite limited. As shown in Table 2, in the I → II transition the unit cell doubles to four molecules, and the symmetry is lowered from tetragonal to orthorhombic. In Raman scattering, one would expect an increase in the number of allowed lattice modes in phase II, since (i) the number of fundamental modes scales with the number of molecules in the

TABLE 1: Raman Frequencies at Ambient Pressure[a]

ν exptl (cm^{-1}) (this work)	ν exptl (cm^{-1}) (refs 24 and 28)	ν calcd (cm^{-1}) (refs 25 and 29)	symmetry (refs 24 and 29)	assignment (ref 29)	dν/dP exptl (cm^{-1}/GPa) (this work)
59	59	39	B_1		−1.8
101	103, 102	110, 107	A_1, E		11.0
134	134	135	E		14.3
174	177	170	E		33.6
547	547	537	A_1	δ CN	8.0
559		565	B_2	δ CN	11.1
572	572	580	E	δ CO	6.3
		589	B_1	τ_s NH_2	
		642	A_2	τ_s NH_2	
715		736	E	τ_a NH_2	
777		797	E	ω CO	
1007		1011	B_2	υ_s CN	
1011	1011	1016	A_1	υ_s CN	12.9
		1065	E	ρ_a NH_2	
1154		1147	B_2	ρ_s NH_2	
1178	1178	1159	A_1	ρ_s NH_2	
1467	1470	1473	E	υ_a CN	
1542	1542	1554	A_1	υ CO	
1597	1580	1613	B_2	υ CO	
1626	1624	1634	E	δ_a NH_2	
1651	1650	1647	A_1	δ_s NH_2	
1680		1685	B_2	δ_s NH_2	
3324	3320	3328	E	υ_s NH_2	1.7
3355	3356	3359	A_1	υ_s NH_2	−1.8
		3343	B_2	υ_s NH_2	
3433	3432	3454	E	υ_a NH_2	−21.5
		3475	B_2	υ_a NH_2	
	3468	3458	A_1	υ_a NH_2	

[a] Lattice modes occur below 300 cm^{-1}. In previous studies, lattice modes were examined in refs 24 (experiment) and 25 (theory), and intramolecular modes in refs 28 (experiment) and 29 (theory). The mode assignments of ref 29 are defined explicitly in ref 30.

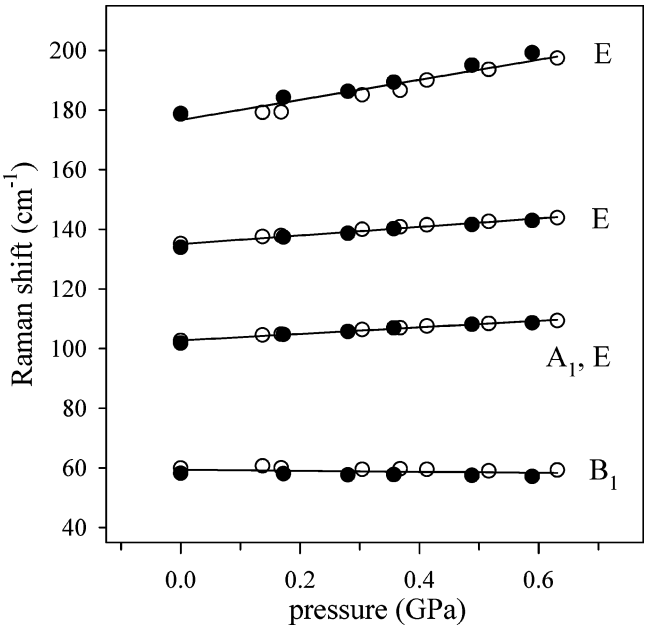

Figure 3. Lattice-mode frequencies as a function of pressure in phase I. The data are from two separate runs. In one case, argon was used as a pressure medium (filled circles), and in the other mineral oil was used (open circles). The solid lines have slopes listed in Table 1.

unit cell and (ii) the drop in symmetry would lead to the lifting of degeneracies in E modes. As can be seen by comparing the phase I and II spectra in Figure 2, a significant increase in the number of lattice modes accompanies the I → II phase transition; 4 and 12 lattice modes were observed in phases I and II, respectively. The number of lattice modes in phase II correlates well with the expected increase associated with the change in symmetry and volume of the unit cell.

The upper plot in Figure 7 shows the decrease in reduced lattice parameters as the pressure is increased in phase II. It is evident that this structure is significantly more compressible along the *b*-axis and stiffer along the *a*- and *c*-axes. From the neutron-scattering results,[13] the phase II structure consists of hydrogen-bonded sheets that are normal to the *b*-axis; our observation of greater compressibility along this axis is consistent with the weaker bonding expected normal to the sheets.

The available neutron data[13] include cell volumes in phases I and II. In the lower plot of Figure 7, we superimpose these data with our results (Table 2) and obtain very good agreement. The combined X-ray and neutron data in phases I and II were fitted with the first-order Murnaghan equation[32]

$$P = \frac{B}{B'}\left[\left(\frac{V_0}{V}\right)^{B'} - 1\right] \qquad (1)$$

where B is the bulk modulus at zero pressure and B' is its derivative. For phases I and II, the fits in Figure 7 yield the moduli $B_I = 8.3$ GPa and $B_{II} = 11.7$ GPa, in approximate agreement with the values $B_I = 10.7$ GPa and $B_{II} = 9.4$ GPa obtained from volumetric measurements.[11] Additional fitting parameters and a comparison with values obtained using the third-order Birch−Murnaghan equation are included in Table 3. The fitting parameters also correspond to a decrease in molecular volume of 6.8% at the I → II phase transition, in good agreement with the 6.95% value given in ref 11.

In addition to the unit-cell dimensions, refinement[23] of the X-ray data indicated that the space group $P2_12_12_1$ (D_2^4) is the best candidate for the phase II space group, consistent with the neutron-scattering results.[14] In this structure, four urea molecules occupy sites with C_1 symmetry. The phase II data also seemed fairly consistent with space group $Pna2_1$ (C_{2v}^9), which also contains four sites with C_1 symmetry.

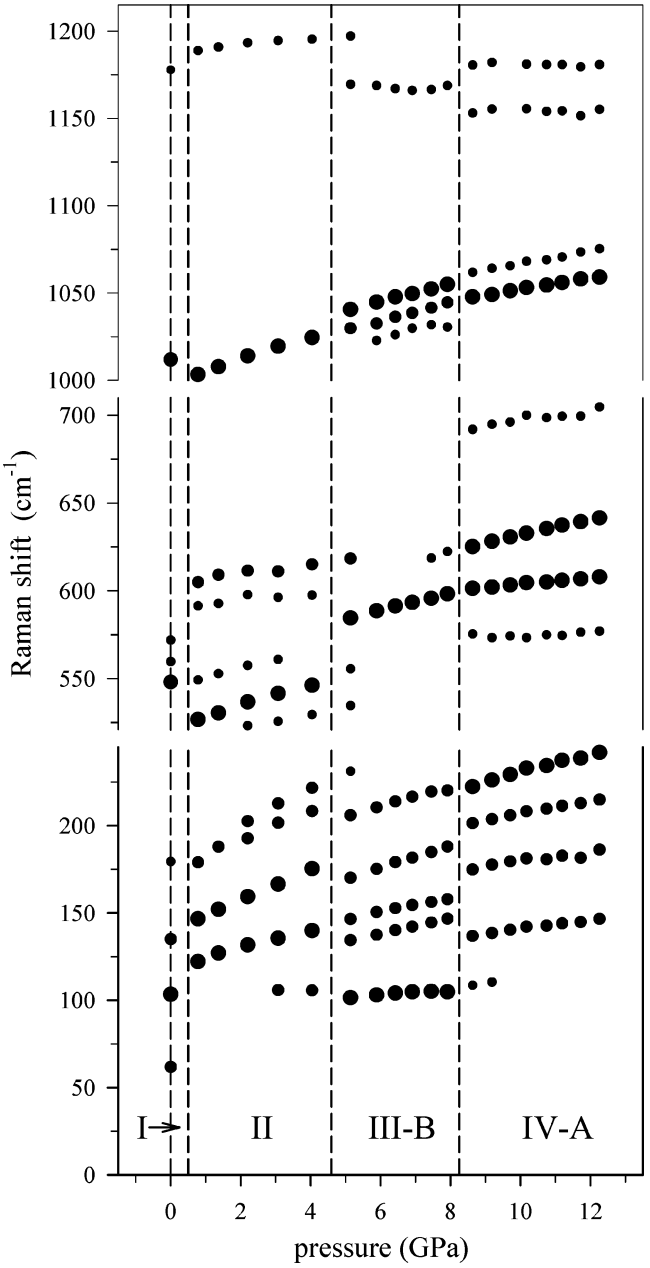

Figure 4. Discontinuities in Raman spectra indicating a sequence of four phases with increasing pressure, for a single-crystal sample in Ar. The three symbol sizes indicate qualitative assignments of intensity as strong, medium, or weak.

The crystallographic structure of phase II has apparently been solved[14] but to our knowledge has yet to appear in print. Theoretical results are also limited. A recent DFT calculation[33] has addressed the structure of urea under high pressure. Because the $P\bar{4}2_1m$ symmetry of the ambient phase was assumed to persist to 10 GPa, no information was provided for higher-pressure phases. In a phenomenological model,[34] the urea structure was allowed to relax, and phase transitions were predicted at approximately 0.1 and 1.2 GPa. Above 1.2 GPa, the predicted space group ($P2_12_12_1$) matches the diffraction results, but the calculated lattice parameters are quite different from those obtained from our X-ray measurements (Table 2).

3.4. Phases III and IV. In Figure 2, it appears that all of the spectra for phases II−IV have approximately the same number of Raman-active modes. According to ref 14, the neutron powder-diffraction data for deuterated urea in phases III and IV can be indexed with orthorhombic unit cells. Because the number of Raman modes would increase if the unit-cell volume doubled or if there was a drop in its symmetry, it is likely that the phase III and IV structures are orthorhombic with 4 molecules per unit cell.

In the third pressure range, single-crystal samples in several runs contained two domains (III-A and III-B) with distinct

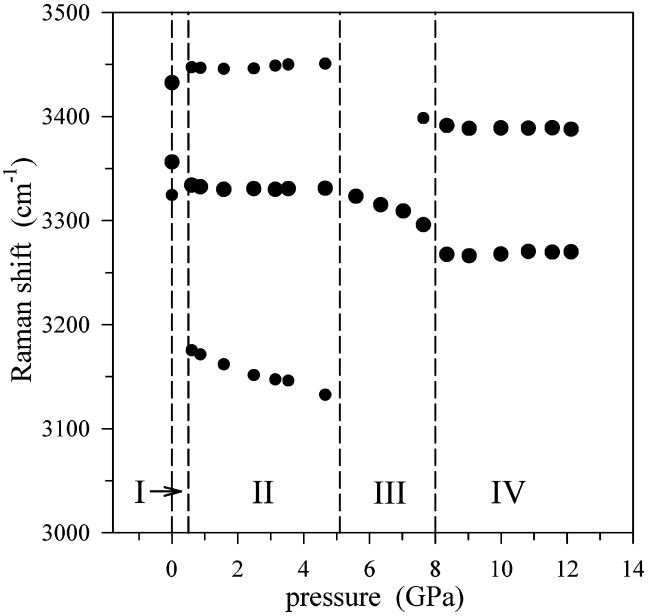

Figure 5. N−H stretching-mode frequencies as a function of pressure, for a single-crystal sample in Ar.

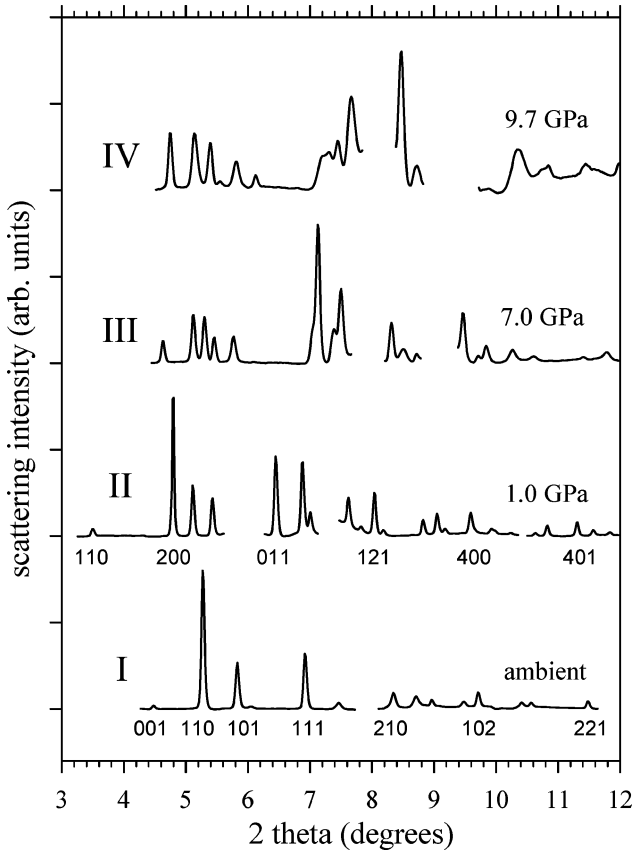

Figure 6. X-ray diffraction patterns for urea phases I−IV. Phase I reflections are indexed in accordance with the known tetragonal ambient structure; phase II is orthorhombic. Only selected indices are shown due to space limitations. Breaks in the diffraction patterns occur near prominent background features. For phases III and IV, the breaks occur at solid-Ar reflections.

TABLE 2: Lattice-Parameter Data for Urea Phases I and II, Obtained Using Data Such as Those Shown in the Lower Two Plots of Figure 6[a]

P (GPa)	*a* (Å)	*b* (Å)	*c* (Å)	V_{cell} (Å^3)	V_{mol} (Å^3)
0	5.65	5.65	4.70	150	75.0
0.5	8.26	3.66	8.85	267	66.9
1	8.24	3.56	8.80	258	64.5
2.2	8.18	3.43	8.71	244	61.1
3.4	8.13	3.34	8.63	234	58.5
4.2	8.13	3.29	8.55	229	57.2

[a] V_{cell} is the unit-cell volume, and V_{mol} is the volume per molecule.

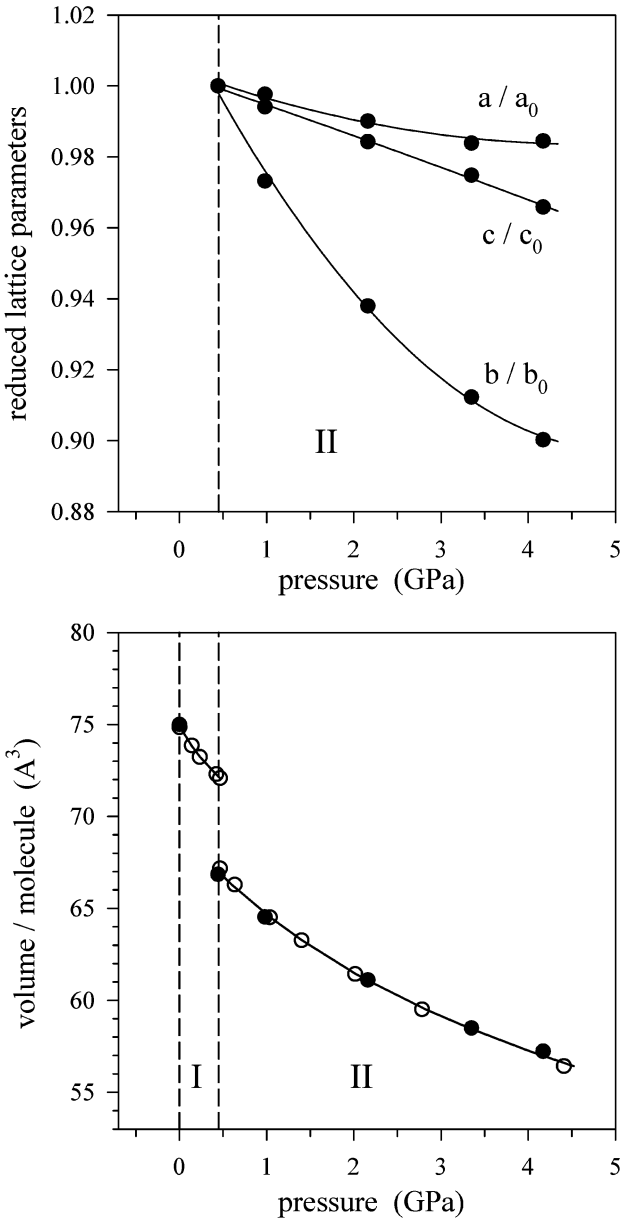

Figure 7. Unit-cell data for urea in phases I and II. (Upper panel) Reduced lattice parameters in phase II, showing anisotropic stiffness. The lines are parabolic fits. (Lower panel) Volume in phases I and II, including data from this study (solid circles) and ref 13 (open circles). The lines are fits to the first-order Murnaghan equation of state.

Raman spectra, as shown by the middle two plots in Figure 2. This effect was observed while translating samples relative to the (fixed) incident laser beam. A very noticeable signature of crossing from one domain to the other is the switching of intensities for the C−N stretching-mode doublet near 1025 cm^{-1}. The splitting of this doublet is approximately 12 cm^{-1} in phase III and 14 cm^{-1} in phase IV, and the positions of the peaks in the doublet are constant over the entire sample. We arbitrarily label the low-frequency peak as A and the high-frequency peak as B, with integrated intensities I_A and I_B. In cases where the sample was very well separated into A and B domains, the switching was nearly complete, i.e., in the A region of the sample $I_A \gg I_B$, and in the B region $I_B \gg I_A$. At boundaries between domains and in single-crystal samples with poor domain separation, we obtained intensities that are more nearly equal: $I_A \approx I_B$. In polycrystalline (powder) samples, there was no evidence of large-scale domain formation; any departures from equal A and B intensities appeared to be confined to individual crystallites.

TABLE 3: Bulk Moduli for Urea Phases I and II[a]

source	B_I (GPa)	B_I'	V_{0-I} (Å^3)	B_{II} (GPa)	B_{II}'	V_{0-II} (Å^3)
first order (M)	8.3	18	75	11.7	6	69.4
third order (B−M)	8.0	24	75	10.8	7	69.5
ref 11	10.7	9.1		9.4	6.7	

[a] The first two rows compare values obtained by fitting the diffraction data of Figure 7 with the first-order Murnaghan equation and the third-order Birch−Murnaghan equation. The data from ref 11 were obtained with a bulk volumetric technique.

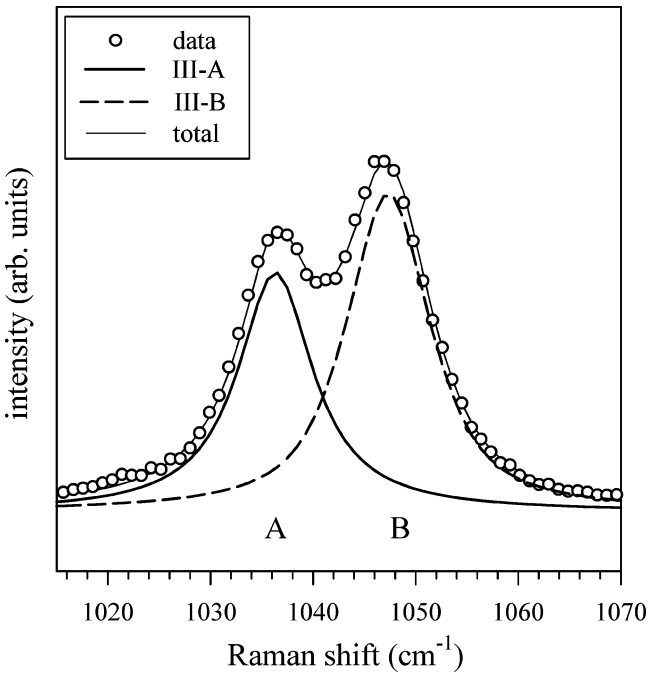

Figure 8. Example of deconvolution of measured intensities into components associated with domains III-A and III-B. The spectrum shown here is one of the ones used to generate Figure 9, part b.

It is convenient to characterize a particular point on a sample by its degree of separation into one domain or the other. To this end, we define the local fraction in domain A as

$$f_A = \frac{I_A}{I_A + I_B} \tag{2}$$

which has limiting values of 1 and 0 when the point is purely in domain A or purely in domain B. Equation 2 was used to characterize the domain composition of samples in phases III and IV; an example showing the deconvolution of a doublet into its components is given in Figure 8.

A sample run with modest domain separation is shown in Figure 9. In Figure 9, part a, a 20 μm grid is superimposed on a sample image; this is the same grid spacing used in the

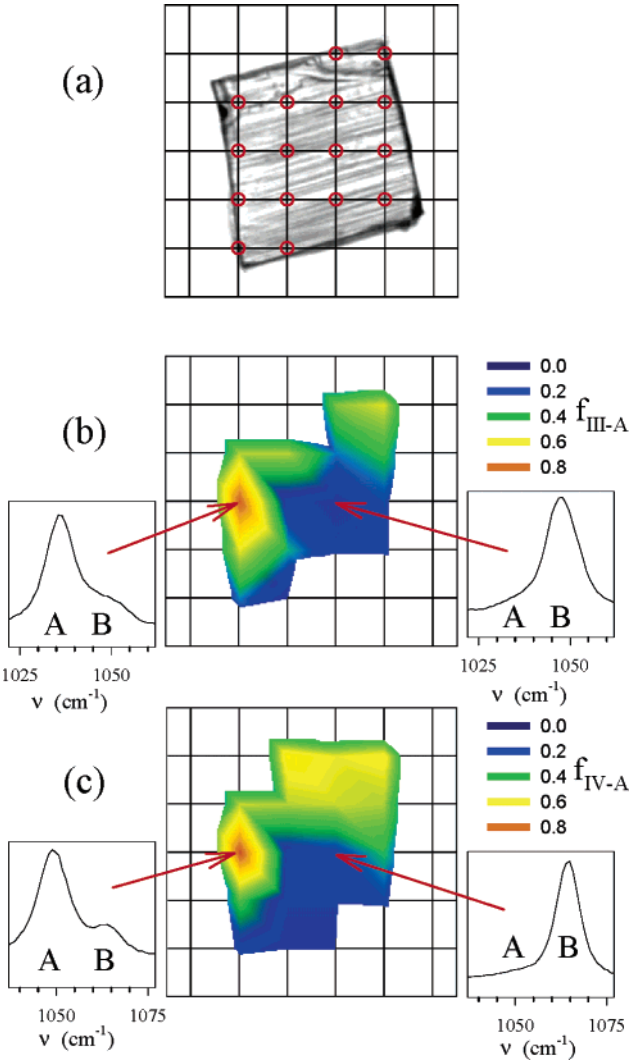

Figure 9. (a) Image of a sample in Ar taken at 9.5 GPa, with an overlaid 20 μm grid. The red circles give the approximate locations where Raman spectra were collected, with diameters corresponding to the 5 μm probe width of the incident laser beam. (b) Raman map collected at 6.6 GPa with portions of the sample in domains III-A and III-B. (c) Raman map collected at 9.3 GPa, showing domains IV-A and IV-B.

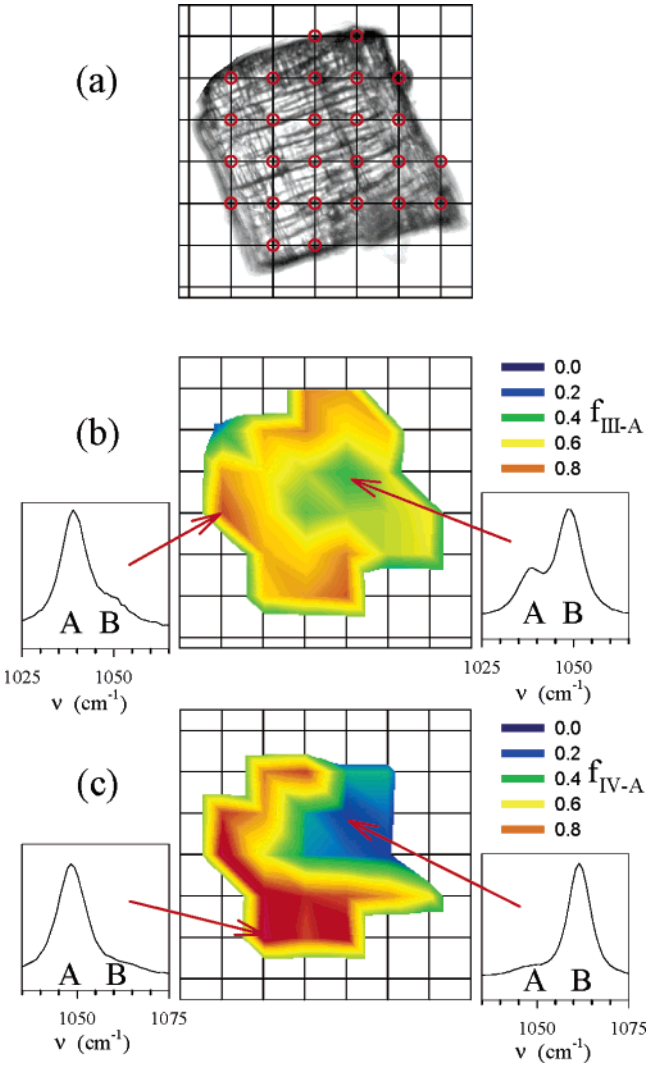

Figure 10. (a) Image of a sample in Ar taken at 0.6 GPa, with an overlaid 20 μm grid. (b) Raman map collected at 7.5 GPa with portions of the sample in domains III-A and III-B. (c) Raman map collected at 9.5 GPa, with domains IV-A and IV-B present.

collection of Raman spectra. Red circles with diameters approximately equal to the width of the incident beam (~5 μm) are shown at the grid points, as a qualitative indication of the locations where the Raman spectra were collected. Since the image was taken after removing the sample from the Raman system, the actual Raman grid may have shifted slightly, relative to the one shown in Figure 9, part a. The horizontal striations seen in Figure 9, part a, are due to the faulting that occurs as a consequence of the large volume reduction during the I → II phase transition.

At 6.6 GPa, the sample is in phase III. Figure 9, part b, is a map of f_{III-A}, the fraction of the sample in phase III-A, obtained by measuring the Raman spectrum at each point on the grid, fitting the measured intensities to obtain I_A and I_B, and applying eq 2. The insets show spectra obtained at specific points on the sample. At points where domain III-A is dominant, $I_A > I_B$, $f_{III-A} > 0.5$, and the map is colored yellow or orange; at points where III-B is dominant, $f_{III-A} < 0.5$, and the map is green or blue.

Figure 9, part c, is a map of f_{IV-A}, the fraction of the sample in domain IV-A, at 9.3 GPa with the sample in phase IV. As with the other runs where Raman maps were generated, the domain geometry in phase IV is similar to that of phase III. That is to say that domain IV-A tended to form in those portions of the sample that had formed domain III-A.

Figure 10 shows another example of domain separation from a different DAC run, plotted with a color scale identical to that of Figure 9. As seen in Figure 10, part a, the faulting in this case, due to the I → II phase transition, was more extensive than in the previous case. The domain separation in phase III was somewhat less developed; no part of the sample contained "pure" domain III-B, as shown by the right-hand inset in Figure 10, part b. However, the separation in phase IV was very well developed, as shown by the color contrast and insets of Figure 10, part c.

Although a comparison of Figures 9 and 10 may lead one to suspect that domain formation becomes more pronounced in samples with larger mechanical faulting, this conclusion was not supported by a comparison of faulting and domain formation in our full set of samples. Any correlation between the two seems to be weak at best.

One could also suspect that domain formation is an artifact arising from pressure gradients in the DAC. However, the results shown in Figures 9 and 10 were obtained under optimal conditions; the pressure medium was Ar, and visual inspection

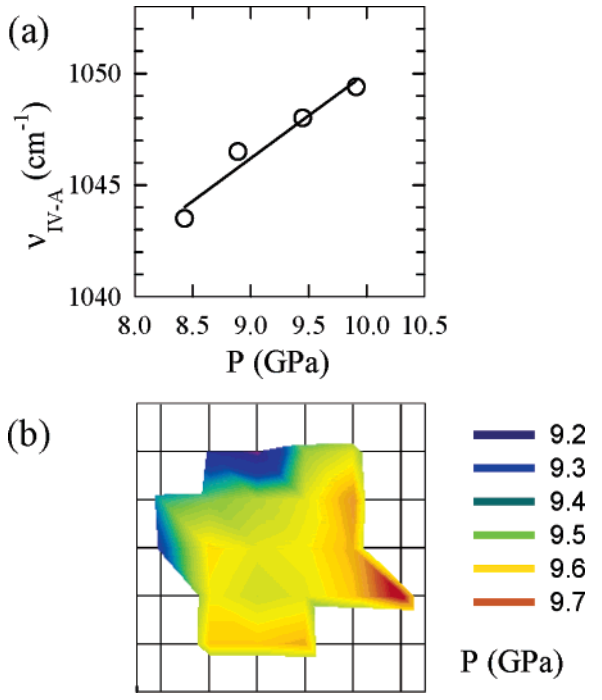

Figure 11. (a) Measured Raman shift vs pressure for the mode associated with phase IV-A (open circles). The line is a fit with a slope of 3.8 cm^{-1}/GPa. (b) Pressure map generated by converting Raman shift to pressure, using the fit from part a. The raw data used in generating this map are those of Figure 10, part c.

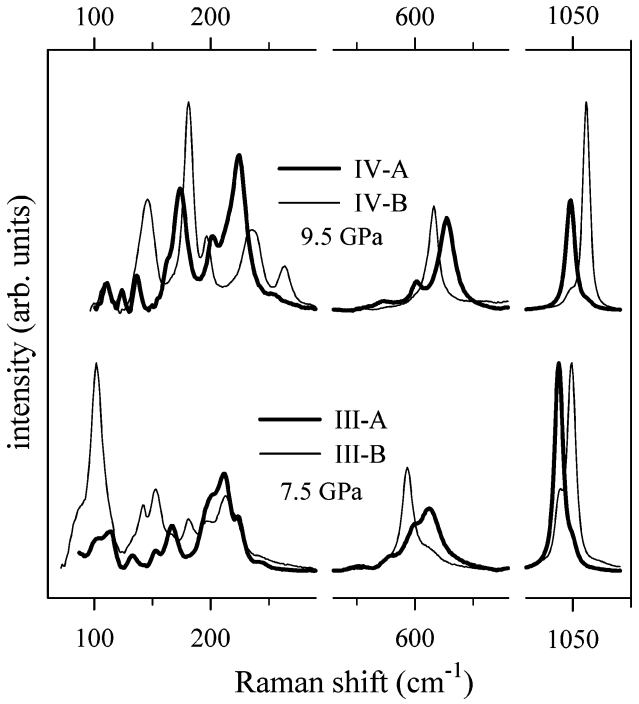

Figure 12. Overlay of A and B Raman spectra in urea phases III and IV, with intensities normalized to allow comparison of spectral features.

of the samples showed that they did not bridge the DAC sample chamber. By monitoring the separation and widths of both R_1 and R_2 ruby lines, we confirmed that quasi-hydrostatic conditions were maintained throughout these experiments.

The pressure distribution *within* the urea crystals was obtained by using the same data set as in the Raman maps. Since pressure gradients should increase with pressure, we take as a worst case the phase IV data of Figure 10, part c, at 9.5 GPa. Each of the two peaks (A and B) that make up the C−N stretching doublet have a pressure dependence. To map the spatial pressure distribution, we first determine the pressure dependence of ν_{IV-A}, the frequency of the A peak in phase IV. This dependence is shown in Figure 11, part a, where $\nu_{IV-A}(P)$ is fit with a straight line. Once this functional relationship is established, we can estimate the pressure at each point by using the measured frequency ν_{IV-A} to calculate $P(\nu_{IV-A})$. The resulting pressure map is shown in Figure 11, part b. During this run, the upper-left corner of the sample was closer to the gasket edge, consistent with the observation of a slightly lower pressure toward the top left and a higher pressure toward the lower right. The pressure variation within the central portion of the sample is no greater than ±0.1 GPa. Furthermore, the spatial distribution of the pressure variation in Figure 11, part b, is not correlated with the domain distribution of Figure 10, part c. On the basis of these results, we conclude that the domain structure shown in Figures 9 and 10 is not due to pressure gradients.

Our definition of f_A in eq 2 is based upon differences in the A and B intensities in a particular doublet. However, as seen in the upper four plots of Figure 2, the A and B domains produce different features across the spectrum: in lattice modes, C−N bending modes (near 600 cm^{-1}), and C−N stretching modes. To understand the physical origin of the A and B domains, it is necessary to make a more detailed evaluation of the differences between the A and B spectra, as discussed below.

We begin by superimposing the A and B spectra in Figure 12, which includes data from the same sample as in Figure 10, at the same pressures. The positions and relative intensities of the peaks in Figure 12 are shown in Table 4. For phase III, which showed modest spatial separation in Figure 10, part b, 10 of the 15 modes in Table 4, part a, are coincident or nearly coincident in frequency for the two domains. This level of matching could indicate that the III-A and III-B spectra arise from the same structure. However, the coincidences could be due to incomplete domain separation, given the modest color contrast of Figure 10, part b. That is to say that if the entire sample contains a mixture of A and B domains smaller than the 5 μm probe size, then the phase III plots in Figure 12 represent a mixture of the two domains.

The phase IV plots in Figure 12 are more distinct. Comparison of the frequencies in Table 4, part b, shows that only 4 of 12 modes are coincident or nearly coincident. This low level of frequency matching and the qualitative differences between the spectra seem more consistent with structurally distinct A and B domains in phase IV.

4. Origin of the Domains in Phases III and IV

The physical origin of the A and B domains observed in urea phases III and IV in our work is an interesting question. It is impossible to completely settle this question with the available data, since, in particular, the crystallographic structures of these phases are unknown. Nonetheless, we discuss the likelihood of different possibilities for the observed behavior.

The first possibility that the A and B domains are an artifact associated with pressure gradients within the sample chamber has been rejected. Another possibility would be the existence of regions with segregated impurities. This effect can most likely be rejected because (i) in all cases, we observed high-quality translation-independent ambient-phase spectra at the beginning and at the end of each DAC run and (ii) there is a good match between our lattice-parameter data and those obtained previously.[3,13]

The A and B domains could be coexisting distinct structural phases, presumably with nearly equal free energies. In equilib-

TABLE 4: Raman Frequencies and Normalized Peak Intensities for Urea Phases III-A and III-B and IV-A and IV-B[a]

(a) Phases III-A and III-B

ν_{III-A} (cm^{-1})	I_{III-A}	ν_{III-B} (cm^{-1})	I_{III-B}
103	0.14	102	0.69
114	0.13		
133	0.06	141	0.16
152	0.06	153	0.25
167	0.19	181	0.14
199	0.27	197	0.12
212	0.33	212	0.18
225	0.17	222	0.11
244	0.02	246	0.03
551	0.01		
581	0.03		
597	0.05	593	0.21
612	0.13	612	0.03
1038	1.00	1038	0.27
1050	0.09	1049	1.00

(b) Phases IV-A and IV-B

ν_{IV-A} (cm^{-1})	I_{IV-A}	ν_{IV-B} (cm^{-1})	I_{IV-B}
111	0.05	109	0.04
124	0.03		
137	0.06	145	0.17
162	0.05		
174	0.20	181	0.31
201	0.10	197	0.10
224	0.23	232	0.07
		240	0.08
		264	0.06
574	0.01		
601	0.03		
627	0.11	616	0.12
1048	0.53	1049	0.07
1063	0.02	1062	1.00

[a] III-A and III-B were derived using the data in the lower plot of Figure 12. IV-A and IV-B were derived using the data in the upper plot of Figure 12.

rium, a single phase would be stable at a given temperature and pressure. However, sluggish transformation kinetics could allow for coexistence in practice. If the coexisting phases are closely related, then one might expect spectral coincidences on the level of those in Figure 12. We reject this possibility on the grounds that it seems very unlikely that such a coexistence would persist over a pressure range of several gigapascals (as occurred in some of our DAC runs). It seems even more unlikely that such a coincidence would occur twice in the same system (in phases III and IV).

We are left with the following conjecture. The A and B domains likely consist of regions with the same crystal structure but with different relative crystallographic orientations. As shown in a detailed polarization analysis of ambient-phase urea single crystals, changes in the scattering geometry can produce quite different spectral features.[35] It is somewhat surprising that differences in sample orientation would produce such a strong effect in our experiment, where all spectra are acquired in backscattering geometry. Nonetheless, this explanation seems the most plausible among those that we have considered.

Finally, we present two possible origins of domains with different orientations. The first involves symmetry breaking during the tetragonal-to-orthorhombic phase I → II transformation. In the tetragonal (ambient-phase) structure, the urea molecules lie in ribbons in the {110} planes. In phase II, the molecules form an orthorhombic structure of sheets[13] that could be parallel to the ribbons in the ambient structure. Since there are two equivalent sets of ribbons, the phase II structure could nucleate in two equally probable domains that are related by a 90° rotation. A similar distribution of rotated domains could occur when phases III and IV are formed. Such an effect would be consistent with our observation that the phase IV domains tend to have a shape similar to the phase III domains, as in Figures 9 and 10.

Another origin of an orientational domain structure would be the formation of rotated ferroelectric domains in single crystals of phases III and IV. Although our data are not explicitly sensitive to ferroelectric ordering, this possibility should be considered, due to the following reasons: the large electric dipole moment of the urea molecule, the noncentrosymmetric ambient-phase structure, and the structural similarity with thiourea, which undergoes ferroelectric ordering below 179 K.[36] The dipole array in the ambient phase of urea can be characterized as antiferroelectric,[2] but net cancellation of the moments might not occur in a lower-symmetry high-pressure phase. Within a given electric domain, polarization would produce asymmetries in the susceptibility tensor that could lead to different Raman spectra for domains with different orientations relative to the incident laser beam.

5. Concluding Remarks

Discontinuities in Raman spectra as a function of pressure indicate that four phases of urea occur at pressures up to 12 GPa. The angle-dispersive X-ray diffraction experiments corroborate the existence of phases I−IV. In phase II, the unit cell doubles relative to the ambient phase and contains four molecules. The I → II phase transition is also accompanied by a drop in symmetry from tetragonal to orthorhombic; the cell size and symmetry changes lead to a significant increase in the number of Raman-active modes in phase II. For phases III and IV, the combined diffraction and Raman data indicate that the unit cells are likely to be orthorhombic with four molecules per unit cell.

Spatially resolved Raman data were used to generate spectral maps of single-crystal samples at high pressure. The maps reveal the formation of A and B domains with significantly different Raman spectra in phases III and IV. Since it seems unlikely that distinct structural phases would coexist over pressure ranges of several gigapascals, we suggest that the spatial domains consist of regions with varying crystallographic orientations or varying directions of electric polarization. Overall, our results reveal a rich and unexpected response to high pressure in a material of fundamental and practical importance.

Acknowledgment. We gratefully acknowledge the help from Dr. C. S. Yoo, Lawrence Livermore National Laboratory (LLNL), in initiating our synchrotron experiments. Drs. H. Cynn (LLNL), W. J. Evans (LLNL), and M. Somayazulu (HPCAT) are thanked for their help during the X-ray measurements. Use of the HPCAT facility was supported by the Department of Energy Basic Energy Sciences, Department of Energy National Nuclear Security Administration (Carnegie/DOE Alliance Center), National Science Foundation, Department of Defense Tank-Automotive and Armaments Command, and the W. M. Keck Foundation. Use of the Advanced Photon Source was supported by the U. S. Department of Energy, Basic Energy Sciences, Office of Science, under Contract No. W-31-109-Eng-38. This work was supported by the Department of Energy (Grant No. DEFG0397SF21388) and Office of Naval Research (Grant No. N000149310369).

References and Notes

(1) Keuleers, R.; Desseyn, H. O.; Rousseau, B.; Van Alsenoy, C. *J. Phys. Chem. A* **1999**, *103*, 4621 and references therein.

(2) Yoshihara, A.; Bernstein, E. R. *J. Chem. Phys.* **1982**, *77*, 5319 and references therein.
(3) Vaughan, P.; Donohue, J. *Acta Crystallogr.* **1952**, *5*, 530.
(4) Kumler, W. D.; Fohlen, G. M. *J. Am. Chem. Soc.* **1942**, *64*, 1944.
(5) Kurtz, S. K.; Perry, T. T. *J. Appl. Phys.* **1968**, *39*, 3798.
(6) Halbout, J. M.; Blit, S.; Donaldson, W.; Tang, C. L. *IEEE J. Quantum Electron.* **1979**, *15*, 1176.
(7) Bridgman, P. W. *Proc. Am. Acad. Arts Sci.* **1916**, *52*, 91.
(8) Hamann, S. D.; Linton, M. *High Temp.*−*High Pressures* **1975**, *7*, 165.
(9) Khilji, M. Y.; Sherman, W. F.; Wilkinson, G. R. In *Raman Spectroscopy, Linear and Nonlinear*; Lascombe, J., Huong, P. V., Eds.; John Wiley & Sons: New York, 1982; p 481.
(10) Andersson, O.; Ross, R. G.; *Int. J. Thermophys.* **1994**, *15*, 513.
(11) Lundin, A.; Ross, R. G.; Bäckström, G. *High Temp.*−*High Pressures* **1994**, *26*, 477.
(12) Yang, G.; Li, Y.; Dreger, Z. A.; White, J. O.; Drickamer, H. G. *Chem. Phys. Lett.* **1997**, *280*, 375.
(13) Bonin, M.; Francis D. J.; Marshall, W.; Toledano, P.; Weber, H.-P. *ISIS/Rutherford Appleton Laboratory Experimental Reports*; http://www.isis.rl.ac.uk/.
(14) Marshall, W. G.; Francis, D. J. *J. Appl. Crystallogr.* **2002**, *35*, 122.
(15) Starting with Bridgman, it has been common to label the first high-pressure phase at ambient temperature as phase III; however, in the following discussion we label the sequence of phases as I, II, III, and IV.
(16) Huang, B.; Su, G.; He, Y. *J. Cryst. Growth* **1990**, *102*, 762.
(17) Merrill, L.; Bassett, W. A. *Rev. Sci. Instrum.* **974**, *45*, 290.
(18) Piermarini, G. J.; Block, S.; Barnett, J. D.; Forman, R. A. *J. Appl. Phys.* **1975**, *46*, 2774.
(19) Barnett, J. D.; Block, S.; Piermarini, G. J. *Rev. Sci. Instrum.* **1973**, *44*, 1.
(20) Park, T.-R.; Dreger, Z. A.; Gupta, Y. M. *J. Phys. Chem. B* **2004**, *108*, 3174.
(21) High Pressure Collarborative Access Team at the Advanced Photon Source at Argonne National Laboratory; http://www.hpcat.aps.anl.gov/
(22) Descriptions of the autoindexing programs and links to them can be found via the Collaborative Computational Project, Number 14, at http://www.ccp14.ac.uk/.
(23) *Materials Studio*, version 3.0; Accelrys: San Diego, CA; http://www.accelrys.com/.
(24) Lefebvre, J.; Fontaine, H.; Fouret, R. *J. Raman Spectrosc.* **1975**, *4*, 173.
(25) Bleckmann, P.; Thibud, M. *J. Mol. Struct.* **1990**, *219*, 7.
(26) Johnson, M. R.; Parlinski, K.; Natkaniec, I.; Hudson, B. S. *Chem. Phys.* **2003**, *291*, 53.
(27) Liapis, K.; Jayasooriya, U. A.; Kettle, S. F. A.; Eckert, J.; Goldstone, J. A.; Taylor, A. D. *J. Phys. Chem.* **1985**, *89*, 4560.
(28) Kutzelnigg, W.; Mecke, R.; Schrader, B.; Nerdel, F.; Kresse, G. *Z. Elektrochem.* **1961**, *65*, 109.
(29) Rousseau, B.; Keuleers, R.; Desseyn, H. O.; Geise, H. J.; Van Alsenoy, C. *Chem. Phys. Lett.* **1999**, *302*, 55.
(30) Rousseau, B.; Van Alsenoy, C.; Keuleers, R.; Desseyn, H. O. *J. Phys. Chem. A* **1998**, *102*, 6540.
(31) Jayaraman, A. *Rev. Mod. Phys.* **1983**, *55*, 65.
(32) Menoni, C. S.; Spain, I. L. In *High-Pressure Measurement Techniques*; Peggs, G. N., Ed.; Applied Science: London, 1983.
(33) Miao, M. S.; Van Doren, V. E.; Keuleers, R.; Desseyn, H. O.; Van Alsenoy, C.; Martins, J. L. *Chem. Phys. Lett.* **2000**, *316*, 297.
(34) Góra, D.; Parlinski, K. *J. Chem. Phys.* **2000**, *113*, 8138.
(35) Durman, R.; Jayasooriya, U. A.; Kettle, S. F. A. *J. Phys. Chem.* **1988**, *92*, 620.
(36) Jona, F.; Shirane, G. *Ferroelectric Crystals*; Pergamon Press: Oxford, 1962.